

Surface boundary-dendrite interactions in thin metallic Al-alloy samples

Maike Becker*, Matthias Kolbe, Sonja Steinbach and Florian Kargl

Institut für Materialphysik im Weltraum, Deutsches Zentrum für Luft- und Raumfahrt (DLR), 51170 Köln, Germany

*Corresponding author. E-Mail address: maike.becker@dlr.de

Crystallographic orientations and growth directions of dendrites in thin Al-15 wt.%Cu (200 μm) and Al-29 wt.%Ge (500 μm) alloys were investigated employing *in situ* X-radiography and post-mortem X-ray tomography and electron backscatter diffraction. The Al-Cu alloy was solidified under microgravity conditions, while the Al-Ge sample was processed horizontally on ground. It was found that (i) dendrites nucleate on both sides of the surface in microgravity, but accumulate under normal gravity near the top surface due to buoyancy, (ii) dendrites grow along preferred in-plane crystallographic directions, which are $\langle 100 \rangle$ for Al-15 wt.%Cu and $\langle 100 \rangle$, $\langle 110 \rangle$ and $\langle 210 \rangle$ for Al-29 wt.%Ge, indicating that the solid-liquid interfacial anisotropy of this Al-Ge composition is similar for these $\langle xy0 \rangle$ directions, (iii) slightly inclined dendrite arms in Al-Cu grow along the sample boundary after contact, whereas tips of inclined dendrite arms in Al-Ge never touch the boundary, but develop new primary tips originating from secondary branches.

Keywords: dendritic growth; surface energy; microgravity; radiography; three-dimensional tomography; electron backscattering patterns

© 2021. This manuscript version is made available under the CC-BY-NC-ND 4.0 license <https://creativecommons.org/licenses/by-nc-nd/4.0/>

Published in Scripta Materialia 209 (2022) 114386: <https://doi.org/10.1016/j.scriptamat.2021.114386>

Interactions between dendritic grains and surfaces take place in casting, especially when thin-walled pieces are produced. To better understand how dendrites in binary metallic alloys develop in confined environments and interact with surfaces, dendritic growth in thin solidified samples is investigated. It is well known that confinement influences grain morphology and growth kinetics [1-7], since the dendrites are not free to grow very far in the preferred direction. The questions remain whether the nucleation position and orientation of dendrites in a confined environment influences the selection of growth directions, what happens when dendrite arms impinge upon a surface, and how it depends on the alloy system.

In near-equilibrium solidification conditions the growth directions of dendrites are controlled by the crystalline anisotropy of the solid-liquid interfacial energy that varies with the orientation of the interface normal with respect to the crystal lattice [8]. The anisotropy is difficult to determine, but is known to be small in the order of 1 % for Al [9-11] and can be easily influenced by alloying elements, e.g. Zn [12]. When alloying alters the anisotropy strength, also the growth morphology of the developing dendrites can change. Depending on the interfacial energy anisotropy as a function of the crystallographic orientation, a different number of dendrite growth directions is possible: 6 for $\langle 100 \rangle$ growth, 8 for $\langle 111 \rangle$ growth, 12 for $\langle 110 \rangle$ growth, or even more growth directions if several crystallographic directions are equally favored. The system Al-Cu predominantly shows $\langle 100 \rangle$ growth directions [13], but in the systems Al-Zn [14] and Al-Ge [15] it was found that compositional changes

lead to a transition of dendrite growth directions from $\langle 100 \rangle$ to $\langle 110 \rangle$. Moreover, it was reported that in the transition composition range arms can grow with textured seaweed structures [16] or along both primary $\langle 100 \rangle$ and $\langle 110 \rangle$ directions if the grain is confined and has a certain orientation with respect to the thin sample geometry [15].

In situ X-ray radiography experiments during the solidification of thin (150–300 μm) metallic Al-alloys are widely used to analyze the nucleation and growth of dendritic grains and arrays [17-26]. The solidifying Al-rich dendrites attenuate less X-rays than the surrounding melt, resulting in contrast in the projection images. For the quantitative analysis of radiography images – often used as reference data for solidification models [5-7, 27-31] – an in depth three-dimensional view of the microstructure evolution in thin samples is required to ensure the correct interpretation of results and the identification and explanation of potential outliers in the data. While from the transmission X-ray contrast some three-dimensional spatial information can be retrieved [5, 32], in general, neither the position of the grains in the beam direction nor their crystallographic growth directions can be identified.

To elucidate the impact of confinement on dendrite nucleation and growth in three dimensions, two samples of compositions Al-15 wt.%Cu and Al-29 wt.%Ge (transition range between $\langle 100 \rangle$ and $\langle 110 \rangle$ [15]) were investigated by performing *in situ* X-radiography, post-mortem tomography and electron backscatter diffraction analysis (EBSD). The samples were cast in a rod-shaped steel crucible from pure elements (6N Al from Hydro, 4N Cu from Alfa Aesar, 4N Ge provided by Leibnitz Institut für Kristallzüchtung in Berlin), cut and ground to the desired thicknesses of 200 μm and 500 μm , respectively. Then the samples were melted and re-solidified in a near-isothermal furnace [33] with a cooling rate of 1 K min^{-1} . This process was recorded by real-time X-radiography. Two X-ray projection image snapshots are shown in Fig. 1(a) and (b) for the Al-Cu and the Al-Ge alloy, respectively. While the Al 15 wt.%Cu sample was processed in microgravity condition on the sounding rocket flight MAPHEUS-7 in the module X-RISE-M [34], the Al-29 wt.%Ge alloy was processed horizontally on ground in the facility X-RISE-G [35]. In order to investigate the orientation of the dendrites in three dimensions, X-ray computed tomography was performed on the solid samples post-mortem with a Phoenix Nanotom 160NF. The reconstructed images have a voxel size of 7 μm^3 and were analyzed with the ImageJ software [36]. Subsequently the samples were prepared for EBSD analysis by polishing with SiC abrasive paper to remove the outer reaction layer followed by mirror polishing with a 0.05 μm Al_2O_3 suspension (MasterPrep® from Buehler). EBSD scans were executed on the scanning electron microscope (SEM) LEO 1530 VP by Zeiss equipped with a Nordlys-2 detector by Oxford HKL. Orientation maps in the sample plane ($x - y$) and normal to the sample surface (z) are displayed using the conventional inverse pole figure (IPF) coloring for a cubic crystal system. Additionally, misorientation maps that show angular deviations from a predefined crystallographic direction are used.

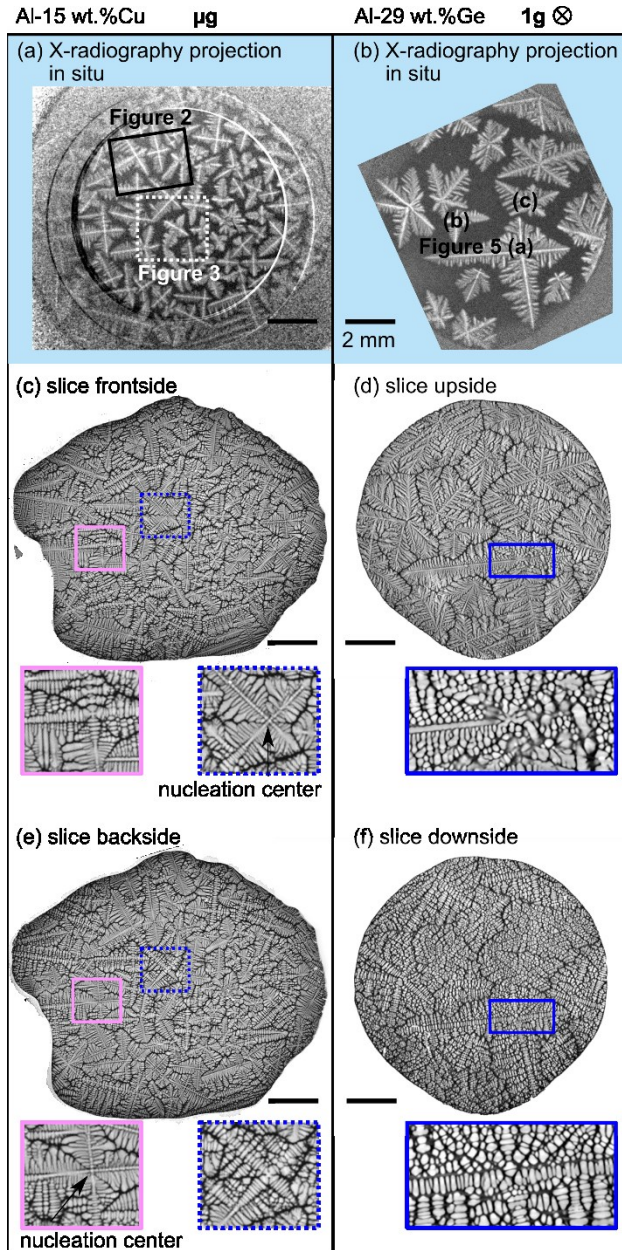


Fig. 1. *In situ* X-radiography images of (a) a 200 μm thin Al-15 wt.%Cu sample solidifying in microgravity (μg) and (b) a 500 μm thin Al-29 wt.%Ge sample solidifying horizontally on ground. (c) and (e) show post-mortem tomography slices close to the front and backside of sample Al-15 wt.%Cu, respectively. Since all grains nucleated and grew in microgravity, there is no difference between up and down. The nucleation centers are located at the sample surfaces on either side. Enlarged areas of two selected dendrites show details of the nucleation centers. The pink solid framed dendrite nucleated at the backside, whereas the blue dotted framed dendrite nucleated at the frontside. (d) and (f) show tomography slices close to the upper and the lower surface of sample Al-29 wt.%Ge, respectively. Many secondary and higher-order branches can be seen at the lower sample boundary, which indicates that the dendrites detached from the lower sample boundary and accumulated at the top. The nucleation centers are closer to or directly at the upper sample boundary. An example can be seen in the supplementary material, in a video showing a series of cuts through the sample thickness from top to bottom and in reverse order.

Tomography slices close to both sample surfaces are shown in Fig. 1(c) and (e) for the Al-15 wt.%Cu sample and in Fig. 1(d) and (f) for the Al-29 wt.%Ge sample. The grain centers in the Al-Cu sample are located equally distributed near one of the two surfaces, whereas in the Al-Ge sample the centers of all grains are located much closer to the upper sample boundary. It shows that first, the sample boundaries trigger nucleation (the Al-Cu sample was solidified in microgravity) and that second, the grains detach from the sample boundary after nucleation and float upward to the surface, when the

sample is processed on ground. This phenomenon results from the lower density of the Al-dendrites, when compared to the interdendritic melt in the Al-29 wt.%Ge sample. It is worth noting that the centers of the dendrites in the Al-Ge sample are not touching the upper surface in many cases. A possible explanation for this observation are dendrite arms that had already developed in the thickness (z-) direction before detachment occurred. A video showing a series of cuts through the sample thickness from top to bottom and in reverse order is included as supplementary material.

The EBSD images in Fig. 2(a) show the crystallographic orientations in standard IPF colors of the dendrites from the black framed area in Fig. 1(a) of the sample Al-15 wt.%Cu from three orthogonal directions (x , y and z), with the z -axis orthogonal to the sample thickness. The colorful images are representative for all dendrites in the sample and directly indicate a wide variety of crystallographic orientations. In Fig. 2(b) the angles of misorientation between the $\{100\}$ crystallographic plane normal directions of the grains closest to the z -axis (denoted $\{100\} \parallel z$) are plotted. EBSD analysis was performed for 65 dendrites, representing 87% of all dendrites in the sample. Compared to the theoretical distribution of randomly oriented grains (black line in Fig. 2(b)), the hypothesis of a “non-random distribution” cannot be rejected (χ^2 test). The random grain distribution used for comparison was simulated with the MTEX Toolbox [37] using 10^6 random oriented grains. Nevertheless, it is possible that smaller misorientation angles $<35^\circ$ prevail in the experiment. It can therefore not be conclusively clarified whether nucleation of Al-grains at the sample boundary favors a special orientation. A more accurate statement could be made with a higher number of grains sampled, but this is difficult because opportunities for experiments in microgravity are rare [34, 38]. What can be stated, however, is that the crystallographic $\{100\}$ plane of most grains nucleated in microgravity is not parallel to the sample plane in the solidified samples, as one might assume by looking only at the projected dendrite morphologies, which in many cases show a four-fold symmetry (see Fig. 1(a)).

The three-dimensional orientation of one particular dendrite (white dotted framed area in Fig. 1(a)) from sample Al-15 wt.%Cu is analyzed in detail in Fig. 3. In general, the grain shows four primary arm growth directions in the radiography projection image, but with different projection intensities of the arms (see Fig. 3(a)). Two opposite arms appear bright and are shorter (blue arrows) compared to the two other arms that are longer and dark at the arm center (orange arrows). Tomographic virtual cuts through the axes of the arms are shown in Fig. 3(b), revealing the arm growth directions with respect to the sample thickness and the nucleation center, which is at or close to the sample boundary. The short bright arms (blue arrows) grow with an angle of 45° to the sample plane and are stopped when they reach the sample boundary. This explains why they are comparatively short and appear bright in the projection image. The other two arms (orange arrows) grow with different angles compared to the sample plane. The left arm (3) grows along the sample boundary, whereas the right arm (4) grows diagonally inside the sample thickness with an angle of 11° to the plane. The crystallographic orientation analysis of this dendrite (Fig. 3(c)) shows that the $\langle 100 \rangle$ directions are inclined from the sample plane by 45° and 11° . It demonstrates that in three cases the arms (1), (2) and (4) grow along $\langle 100 \rangle$. Only the arm (3) deviates from the crystallographic $\langle 100 \rangle$ growth direction, simply because it is mechanically confined by the sample boundary and is forced to grow along another direction, in this case along the sample boundary. Nevertheless, its secondary branches retain a $\langle 100 \rangle$ growth direction (90° angle to the primary arm). The orientation relationship also explains why the center of two arms (orange arrows) appear dark: as the secondary branches grow along the remaining $\langle 100 \rangle$ directions that are not parallel to a z -plane direction (the same or opposite directions as (1) and (2)), there is less solid Al and more melt above and below the primary arms, which reduces the brightness in the projection image.

The position of the dendrite is very similar to the proposed three-dimensional dendrite orientation in a similar experiment [23] modeled by Olmedilla et al. [5], who assumed such an inclined orientation based only on the analysis of the transmission X-ray contrast. The analysis shown here confirms the correct interpretation of the transmission X-ray contrast. Additionally, the analysis

presented here reveals that dendrite arms in Al-15 wt.%Cu grow exclusively along $\langle 100 \rangle$ and kink if they are constrained by the sample surface.

Kinking and subsequent growth of dendrite arms along the sample boundary was frequently observed when the crystallographic $\langle 100 \rangle$ direction was not parallel to the sample plane. Further examples of this growth behavior are shown in Fig. 4. There could be a correlation between the magnitude of the angle between an arm and the sample boundary, and the fact whether the arm stops growing or kinks and follows the sample boundary. Roughly estimated by measuring the angles between the dendrite arms and the sample boundary in Fig. 4, this threshold could be between 18 and 22° .

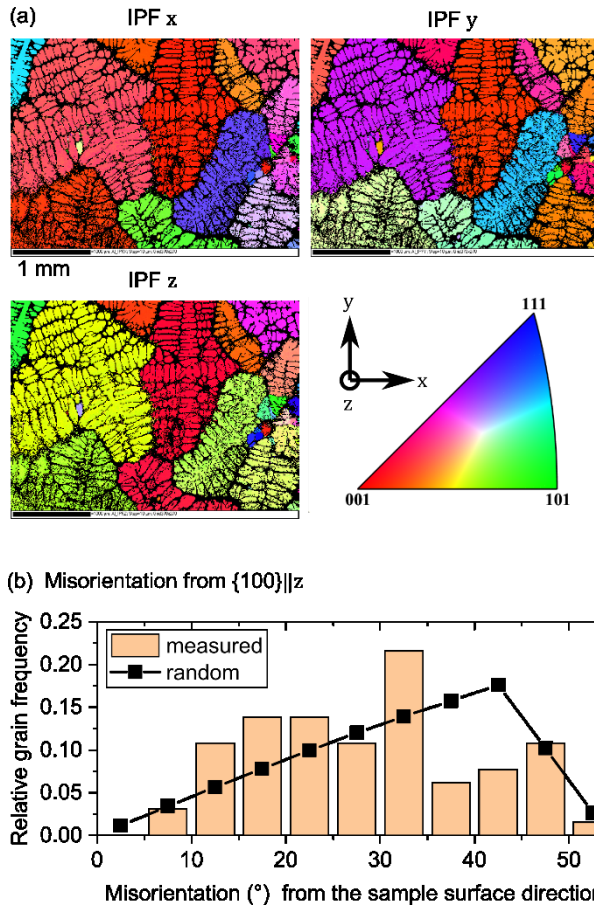


Fig. 2. (a) IPF x , IPF y and IPF z grain orientation maps obtained by EBSD measurements of the black framed area in Fig. 1(a) of sample Al-15 wt.%Cu. (b) The graph shows the measured angle of misorientation between the closest $\langle 100 \rangle$ -direction and the z -direction (normal of the sample surface) for 65 dendrites in the sample. The black line represents the misorientation angle distribution for randomly oriented grains using the same bin size of 11° .

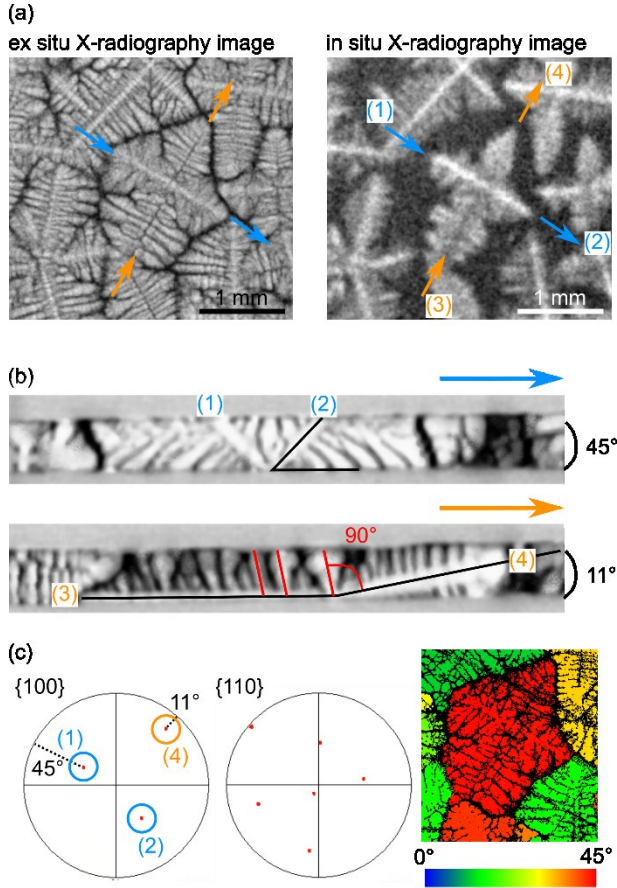


Fig. 3. (a) Detailed ex situ and *in situ* X-radiography images of the white dotted area in **Fig. 1(a)** of the Al-15 wt.%Cu sample. (b) Virtual tomographic cuts parallel to *z* through the arm centers of a selected dendrite. (c) Grain orientation of the red dendrite shown in {100} and {110} stereographic projections. In the image on the right, the misorientation between the $\langle 100 \rangle$ -direction and the *z*-axis ($\{100\} \parallel z$) is represented in color, where blue corresponds to zero misorientation and red corresponds to a misorientation angle of 45°.

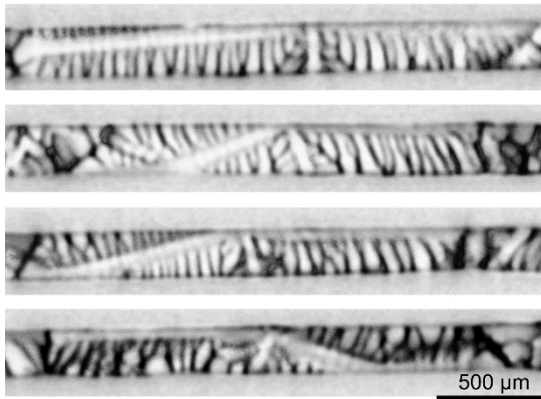


Fig. 4. Virtual tomographic vertical cuts along several primary dendrite arms in the sample Al-15 wt.% Cu. One arm grows along the sample boundary, while the opposite arm grows inclined inside the thickness of the sample following the crystallographic $\langle 100 \rangle$ direction as explained in Fig. 3 and in the text. After contact with the surface due to spatial constraints, it kinks and also follows the surface. The secondary branches grow into the sample until touching the surface.

Crystallographic dendrite growth directions are more variable in the Al-Ge system. In the transition composition region, around 25-29 wt.%Ge, $\langle 100 \rangle$ and $\langle 110 \rangle$ directions were observed [15]. This would lead to 18 options for the growth direction. Fig. 5 clearly shows that different growth

directions develop depending on the orientation of the grain with respect to its spatial conditions. In fact, the arms of the dendrites always try to grow along crystallographic directions that are closest to the sample plane. The crystallographic growth directions were derived from the stereographic projections that in this case represent the lower hemispheres, because the nucleation centers are closer to the upper sample boundary and the arms grow initially downwards. The selected growth directions are encircled in the stereographic projections of Fig. 5. In the case of dendrites (a) and (b), it results in mixed $\langle 100 \rangle$ and $\langle 110 \rangle$ primary arm growth, and in case of dendrite (c) in pure $\langle 110 \rangle$ growth. Moreover, for dendrite (b), the growth of a $\langle 210 \rangle$ dendrite arm is observed that grows diagonally between the primary arms. When the preferred growth directions are not oriented perfectly parallel to the sample plane (have an angle of more than 3° to the sample plane), as is the case for the arms (II)2 and (I)4 of dendrite (a), the primary arms grow up and down in a zigzag manner (see vertical tomographic cuts of Fig. 5(a)). The arm (II)2 grows along a $\langle 110 \rangle$ direction, because it is the closest low-index in-plane direction with an angle of only 4° . When its primary dendrite tip approaches the surface, a new primary tip develops out of a secondary dendrite arm and follows the same growth direction. Note that the arm (II)2, which is enclosed by a yellow dotted line, has a different crystallographic orientation than the rest of the dendrite. It broke off near the dendrite center shortly after nucleation, which can be concluded from the *in situ* X-ray observation. The lower arm (I)4 shows a similar branching behavior, but grows preferentially along $\langle 100 \rangle$, although the direction is inclined by 15° from the sample plane. The variety of possible growth directions indicate that the anisotropy of the solid-liquid interfacial energy is similar in $\langle 100 \rangle$, $\langle 110 \rangle$ and $\langle 210 \rangle$ for the alloy composition Al-29 wt.%Ge and that the interactions with the sample boundary influence the directions of growth. As a consequence, this analysis shows that experimental observation of dendrite growth directions can provide qualitative information on the strength of the solid-liquid anisotropy in a system.

What distinguishes the observations made in the Al-Cu and the Al-Ge samples is the growth of dendrite arms along the sample boundary, which occurs in the case of Al-Cu when the preferred $\langle 100 \rangle$ crystallographic growth direction is not in the sample plane, but which was not observed in Al-Ge. This difference could be related to the propagation velocity of the diffusion field in front of a dendrite tip. The diffusion field propagation is faster for Al-Ge [39] in comparison to Al-Cu [40], which leads to an early interaction of the solute layer with a surface and stops the tip growth in front of a boundary. As a consequence, the arms in Al-Ge might not grow along the boundary, in contrast to what is observed in Al-Cu. Moreover, dendrites in Al-29 wt.%Ge exhibit more possible growth directions than dendrites in Al-Cu and can therefore choose to grow along another suitable growth direction. Tip splitting or hyperbranched growth was rarely observed in both systems, which indicates that the anisotropy is pronounced in certain directions and that the solid-liquid interfacial energy is strong enough to stabilize the tips. Furthermore, the contact angle between a dendrite arm and the boundary could play a role in the interaction behavior.

In addition, the findings show that measurements of dendrite tip growth velocities must concentrate on dendrite arms having in-plane growth directions when comparisons with simulations are pursued. Based on the Al-Ge experiment presented here, it is assumed that dendrites with in-plane growth directions have the fastest growing tips (see left arm in Fig. 5(a)). Whether tip growth along a sample boundary results in faster tip growth rates, as was modeled by Rappaz et al. [41] and Olmedilla et al. [42], could not be confirmed and depends on the wetting behavior. More systematic studies considering grain orientations, neighboring dendrites and boundary wetting conditions would be needed for this purpose. This study shows that the microstructure development of dendrites even in confined geometries is very complex and that projection images should be analyzed extensively.

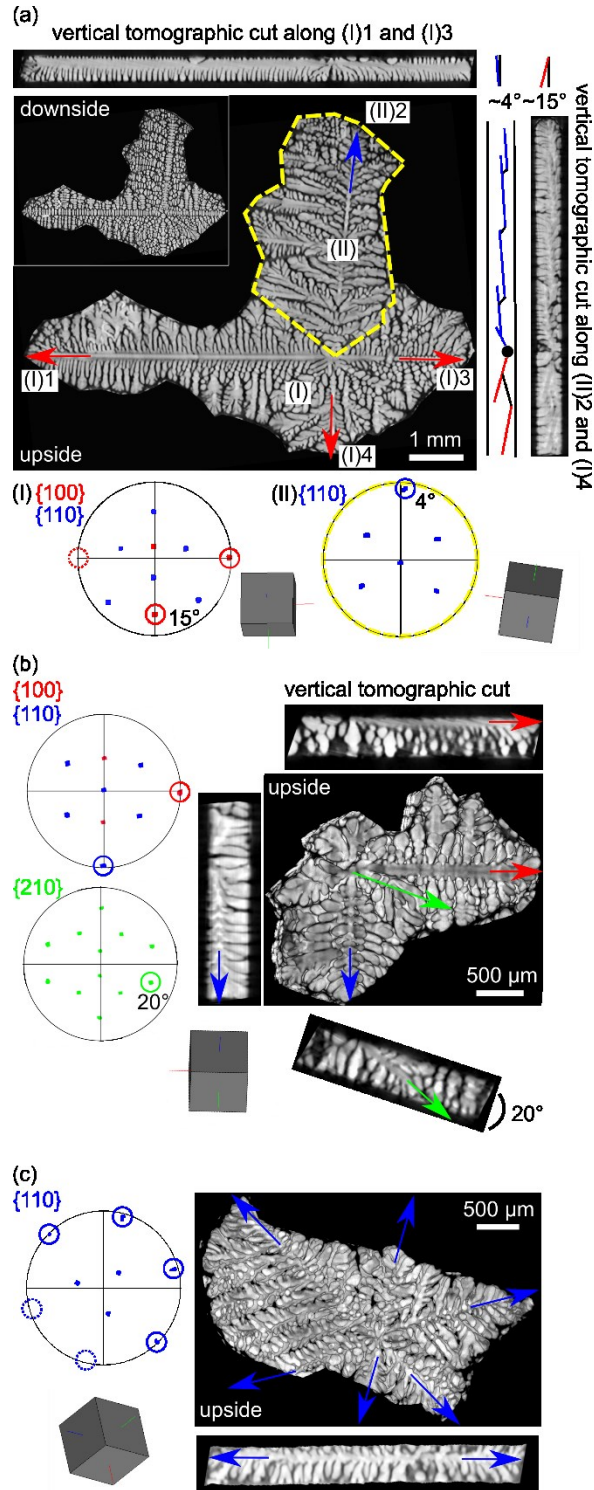


Fig. 5. Crystallographic dendrite arm growth directions and three-dimensional arm orientations analyzed for three dendrites of the sample Al-29 wt.%Ge. From the stereographic projections it can be seen that the dendrites show approximately the three main orientations, with (a) the {100}, (b) the {110} and (c) the {111} planes oriented parallel to the sample plane. The stereographic projections represent the lower hemispheres. The arm (II)2 of dendrite (a), outlined by a yellow dotted line, has a different orientation than the rest of the dendrite. This arm probably broke off early during its growth. The dendrites select those low-indexed growth directions for their primary arms that are closest to the sample plane. These are $\langle 100 \rangle$ and $\langle 110 \rangle$ for dendrite (aI) and (aII), respectively, $\langle 100 \rangle$ and $\langle 110 \rangle$ for dendrite (b) and $\langle 110 \rangle$ for dendrite (c). The variety of directions indicates that the anisotropy strength of the solid-liquid energy is very similar in those directions.

Acknowledgments

We thank our colleagues from DLR T. Werner and T. Volkmann for fruitful discussions and proof reading and A. Jafarizadeh for his help operating the Nanotom facility. Moreover, we thank the teams of DLR Mobile Rocket Base (MORABA) and Swedish Space Corporation (SSC) for their excellent service in making the MAPHEUS campaigns a success. We thank J. Drescher and M. Wegener, respectively, for the preparation of the X-RISE-M facility and the samples for the sounding rocket flight.

Supplementary materials

Supplementary material associated with this article can be found, in the online version, at doi:10.1016/j.scriptamat.2021.114386.

References

- [1] M.E. Glicksman, R.J. Schaefer, J.D. Ayers, *Metall Trans A* 7 (1976) 1747-1759.
- [2] G.A. Alfintsev, G.P. Chemerinsky, O.P. Fedorov, *Krist Tech* 15 (1980) 643-648.
- [3] A.J. Clarke, D. Tournet, Y. Song, S.D. Imhoff, P.J. Gibbs, J.W. Gibbs, K. Fezzaa, A. Karma, *Acta Mater* 129 (2017) 203-216.
- [4] A.K. Boukellal, J.-M. Debierre, G. Reinhart, H. Nguyen-Thi, *Materialia* 1 (2018) 62-69.
- [5] A. Olmedilla, M. Zaloznik, H. Combeau, *Acta Mater* 173 (2019) 249-261.
- [6] W.U. Mirihanage, K.V. Falch, D. Casari, S. McFadden, D.J. Browne, I. Snigireva, A. Snigirev, Y.J. Li, R.H. Mathiesen, *Materialia* 5 (2019) 100215.
- [7] M. Becker, L. Sturz, D. Bräuer, F. Kargl, *Acta Mater* 201 (2020) 286-302.
- [8] M. Asta, C. Beckermann, A. Karma, W. Kurz, R. Napolitano, M. Plapp, G. Purdy, M. Rappaz, R. Trivedi, *Acta Mater* 57 (2009) 941-971.
- [9] R.E. Napolitano, S. Liu, *Phys Rev B* 70 (2004) 214103.
- [10] J.R. Morris, *Phys Rev B* 66 (2002) 144104.
- [11] S. Liu, R.E. Napolitano, R. Trivedi, *Acta Mater* 49 (2001) 4271-4276.
- [12] T. Haxhimali, A. Karma, F. Gonzales, M. Rappaz, *Nat Mater* 5 (2006) 660-4.
- [13] J. Strickland, B. Nenchev, H. Dong, *Crystals* 10 (2020) 627.
- [14] F. Gonzales, M. Rappaz, *Metall Trans A* 37 (2006) 2797-2806.
- [15] M. Becker, J.A. Dantzig, M. Kolbe, S.T. Wiese, F. Kargl, *Acta Mater* 165 (2019) 666-677.
- [16] J. Friedli, J.L. Fife, P. Di Napoli, M. Rappaz, *Metall Trans A* 44 (2013) 5522-5531.
- [17] E.W.J. Miller, M.P. Stephenson, J. Beech, *J Phys E: Sci Instrum* 8 (1975) 33-37.
- [18] J.N. Koster, *Jom* 49 (1997) 31-35.
- [19] R.H. Mathiesen, L. Arnberg, F. Mo, T. Weitkamp, A. Snigirev, *Phys Rev Lett* 83 (1999) 5062-5065.
- [20] S. Boden, S. Eckert, B. Willers, G. Gerbeth, *Metall Trans A* 39 (2008) 613-623.
- [21] D. Ruvalcaba, R.H. Mathiesen, D.G. Eskin, L. Arnberg, L. Katgerman, *Metall Trans B* 40 (2008) 312-316.
- [22] R.H. Mathiesen, L. Arnberg, H. Nguyen-Thi, B. Billia, *Jom* 64 (2012) 76-82.
- [23] A.G. Murphy, R.H. Mathiesen, Y. Houltz, J. Li, C. Lockowandt, K. Henriksson, G. Zimmermann, N. Melville, D.J. Browne, *J Cryst Growth* 440 (2016) 38-46.
- [24] Y.J. Xu, D. Casari, Q. Du, R.H. Mathiesen, L. Arnberg, Y.J. Li, *Acta Mater* 140 (2017) 224-239.
- [25] H. Yasuda, Y. Yamamoto, N. Nakatsuka, M. Yoshiya, T. Nagira, A. Sugiyama, I. Ohnaka, K. Uesugi, K. Umetani, *Int J Cast Metal Res* 22 (2013) 15-21.
- [26] N. Shevchenko, J. Grenzer, O. Keplinger, A. Rack, S. Eckert, *Int J Mat Res* 111 (2020) 11-16.
- [27] S. McFadden, P.L. Schaffer, R.H. Mathiesen, D.J. Browne, *Mater Sci Forum* 654-656 (2010) 1359-1362.
- [28] G. Reinhart, C.A. Gandin, N. Mangelinck-Noël, H. Nguyen-Thi, J.E. Spinelli, J. Baruchel, B. Billia, *Acta Mater* 61 (2013) 4765-4777.

- [29] Y. Chen, D.Z. Li, B. Billia, H. Nguyen-Thi, X.B. Qi, N.M. Xiao, ISIJ Int 54 (2014) 445-451.
- [30] M. Ahmadein, M. Wu, G. Reinhart, H. Nguyen-Thi, A. Ludwig, IOP Conf Ser: Mater Sci Eng 117 (2016) 012010.
- [31] X.B. Qi, Y. Chen, X.H. Kang, D.Z. Li, Adv Mater Sci Eng 2016 (2016) 1-10.
- [32] W.U. Mirihanage, K.V. Falch, I. Snigireva, A. Snigirev, Y.J. Li, L. Arnberg, R.H. Mathiesen, Acta Mater 81 (2014) 241-247.
- [33] M. Becker, C. Dreissigacker, S. Klein, F. Kargl, Rev Sci Instrum 86 (2015) 063904.
- [34] F. Kargl, J. Drescher, C. Dreissigacker, M. Balter, M. Becker, M. Wegener, E. Sondermann, Rev Sci Instrum 91 (2020) 013906.
- [35] S. Klein, D. Bräuer, M. Becker, A. Knipstein, S. Meckel, E. Sondermann, F. Kargl, Int J Microgravity Sci Appl 33 (2016) 330405.
- [36] W.S. Rasband, <https://imagej.nih.gov/ij/>, National Institutes of Health, Bethesda, Maryland, USA, 1997-2018.
- [37] F. Bachmann, R. Hielscher, H. Schaeben, Sol St Phen 160 (2010) 63-68.
- [38] A.G. Murphy, R.H. Mathiesen, Y. Houltz, J. Li, C. Lockowandt, K. Henriksson, N. Melville, D.J. Browne, J Cryst Growth 454 (2016) 96-104.
- [39] R.A. Khairulin, S.V. Stankus, P.P. Bezverkhy, J Alloy Compd 312 (2000) 211-218.
- [40] E. Sondermann, N. Jakse, K. Binder, A. Mielke, D. Heuskin, F. Kargl, A. Meyer, Phys Rev B 99 (2019) 024204
- [41] M. Rappaz, J. Friedli, A. Mariaux, M. Salgado-Ordorica, Scripta Mater 62 (2010) 904-909.
- [42] A. Olmedilla, M. Zaloznik, M.C. Fernández, A. Viardin, H. Combeau, IOP Conf Ser: Mater Sci Eng 529 (2019) 012040.